Advanced Powder Technology 34 (2023) 104272

Contents lists available at ScienceDirect

Advanced Powder Technology

journal homepage: www.elsevier.com/locate/apt

A comparative study of the fixed pivot technique and finite volume schemes for multi-dimensional breakage population balances

Suet Lin Leong [a], Mehakpreet Singh [b], Firnaaz Ahamed [c,d], Stefan Heinrich [e], Simon Ing Xun Tiong [a], Irene Mei Leng Chew [a,f], Yong Kuen Ho [a,f,*]

[a] Department of Chemical Engineering, School of Engineering, Monash University Malaysia, Jalan Lagoon Selatan, 47500 Bandar Sunway, Selangor, Malaysia
[b] Mathematics Applications Consortium for Science and Industry (MACSI), Department of Mathematics and Statistics, University of Limerick, Limerick V94T9PX, Ireland
[c] Department of Biological Systems Engineering, University of Nebraska–Lincoln, Lincoln, NE, USA
[d] School of Engineering, Faculty of Innovation and Technology, Taylor's University, 47500 Subang Jaya, Selangor, Malaysia
[e] Institute of Solids Process Engineering and Particle Technology, Hamburg University of Technology, Denickestraße 15, 21073 Hamburg, Germany
[f] Monash-Industry Plant Oils Research Laboratory (MIPO), Monash University Malaysia, Jalan Lagoon Selatan, 47500 Bandar Sunway, Selangor, Malaysia

ARTICLE INFO

Article history:
Received 19 August 2023
Received in revised form 11 October 2023
Accepted 1 November 2023

Keywords:
Multi-dimensional Population Balances
Breakage
Fixed pivot technique
Finite volume schemes

ABSTRACT

When modeling particle breakage, the use of a single dimension to characterize particulate systems becomes intractable when multiple dimensions (e.g., size and shape) are important. Amongst many potential numerical techniques, the Fixed Pivot Technique (FPT) and Finite Volume Schemes (FVS) are popular choices to resolve multi-dimensional breakage population balance equations (PBEs). However, whether there exists a general multi-purpose technique between the two remains unclear. Across all test cases with identical size domain and mesh, while both techniques demonstrate comparable accuracy in resolving the moments and number densities (with maximum difference in average relative errors of $\sim O(10^0)$ and $\sim O(10^2)$, respectively), and exhibit similar computational efficiency (time taken by FPT relative to FVS is of $\sim O(10^0)$), the choice of numerical technique is contingent upon the properties where accurate prediction is critical. To this end, FVS is the preferred choice when precise estimation of up to two properties is required owing to its simplicity, albeit requiring distinct schemes for different properties. Conversely, when more than two properties are crucial, the FPT is more suited as it preserves up to four properties in the internal 2D space. Overall, this work offers rational guidance for efficient and accurate modeling of multi-dimensional breakages.

1. Introduction

Underlying one of the common occurrences of the universe, is the break-up of particles, a phenomenon that is both rich and intricate. Breakage or fragmentation yields the creation of two or more smaller daughter particles from a larger parent particle, spanning across a multitude of scenarios, e.g., in depolymerization [1–4], granulation [5], milling [6], grinding [7], sonication [8,9], cell division [10], and droplet break-up [11]. These processes entail particles dispersed along an internal parameter, such as size, undergoing a transformative shift in distribution as they cascade into smaller, fragmented entities. To this end, the Population Balance Equation (PBE), which is the fundamental number-conserving equation, is the natural choice to model the evolution of particle distributions [12–16].

While the use of a single internal coordinate (e.g., volume-equivalent diameter) to characterize a particulate system is common and convenient [1,3,4], crucial characteristics of particulate system are often multi-dimensional. For instance, the production of active pharmaceutical ingredients (API) with high aspect ratio [17–23], or cellulose nanocrystals with desired morphology for specific applications [24], necessitates careful control over both the size and shape of the particles. Moreover, comprehending the minimum energy required to fracture a particle of a specific size for comminution necessitates meticulous examination of two distinct properties [5]. Therefore, in cases where tracking the behavior of a particle population with two internal coordinates is crucial, a traditional one-dimensional PBE is no longer adequate, rendering the use of a two-dimensional (2D) or Bivariate Population Balance Model (2D-PBM) [17–23]. Leveraging 2D-PBMs for breakage pro-

* Corresponding author at: Department of Chemical Engineering, School of Engineering, Monash University Malaysia, Jalan Lagoon Selatan, 47500 Bandar Sunway, Selangor, Malaysia.
E-mail address: ho.yongkuen@monash.edu (Y.K. Ho).

https://doi.org/10.1016/j.apt.2023.104272

Nomenclature

$a, b, c,$ and d	Particle fractional assignments
C_{ij}	Cell ij
M_x	Number of grid points in the horizontal x direction
M_y	Number of grid points in the vertical y direction
$M_{\lambda\mu}(t)$	Moments of order $\lambda\mu$
$n(v, w, t)$	Number density of particles (v, w)
$\bar{n}_{ij}^{num}(t)$	Numerical cell average number density of ij - th grid point/pivot
$\bar{n}_k$	cell average number density of k - th grid point/pivot sorted in descending order with respect to the analytical solution
$N_{ij}(t)$	Total number of particles in ij - th cell
Q_m	Quadrant m surrounding pivot $\left(x_i, y_j\right)$
$v,\ w$	Continuous particle sizes
$v',\ w'$	Continuous parent particle sizes, where $v' \geqslant v$ and $w' \geqslant w$
$v_i,\ v_{i+1},\ w_j,\ w_{j+1}$	Cell limits of ij - th cell
$\bar{v},\ \bar{w}$	Average particle sizes
$x_i,\ y_j$	Grid point/pivot coordinates of ij - th cell
t	Time
Greek symbols	
$\beta(v, w, v', w')$	Stoichiometric kernel
$\Gamma(v, w)$	Breakage rate kernel
δ	Dirac-delta function
$\Delta v_i,\ \Delta w_j$	Width of ij - th cell
$\varepsilon(t)$	Time-specific grid-averaged relative number density error
$\sigma_{\lambda\mu}$	Time-averaged relative moments error
η_{ijpq}^{num}	Particle allocation function for birth terms
φ_{ij}^{num}	Particle allocation function for death terms

cesses, such as the production of API in the pharmaceutical industry, has allowed for significant time and resource-saving by mitigating the need for trial-and-error in tuning process parameters to control the particle aspect ratio [20].

Solving multi-dimensional PBEs is a non-trivial task fraught with complexities due to their integro-partial differential nature. Although computing capacities have greatly improved in the modern-day environment, being able to solve multi-dimensional PBEs efficiently and accurately is still advantageous in situations which involve online monitoring, optimization, and control where high sampling rate is required. In this regard, the use of accurate and efficient numerical techniques is almost necessary as analytical solutions are a rare find. The common numerical techniques for solving multi-dimensional PBEs include the Fixed Pivot Technique (FPT) [25–29], Cell Average Technique (CAT) [30,31], Finite Volume Schemes (FVS) [32–38], Method of Moments (MOM) [39,40], and Monte-Carlo schemes [40,41]. Amongst these techniques, MOM is primarily designed to resolve only the dynamics of moment-related quantities, which requires additional processing steps to obtain the number distribution, while the use of Monte-Carlo incurs higher computational expense [42]. Further, the CAT was devised to resolve the overprediction by the FPT [30], which is particularly more significant in aggregation problems compared to breakage [30,43,44]. Among the different FVS variants developed for solving multi-dimensional breakage, the schemes developed by Saha et al. [35] have emerged as attractive options due to their simplicity and excellent accuracy.

To this end, the FPT and FVS have emerged as appealing techniques for solving pure multi-dimensional breakage PBEs, owing to their ability to accurately predict the transients of the complete number density and moments with reasonable computational efficiency. Nevertheless, a comprehensive and objective comparison of their performances is currently lacking. For instance, most FVS-based studies explored only the prediction of moment-related quantities [34,35,45] and neglected the number densities in their analyses. Moreover, 2D FPT implementations using rectangular [25,29,30,46], triangular [26], and radial [27,28] grids were only investigated for pure aggregation and simultaneous aggregation and breakage problems. Pure breakage problems, in this regard, were not adequately studied. Although Nandanwar and Kumar [27] included 2D FPT for pure breakage, their study considered only a limited number of case studies involving binary breakage with size-dependent breakage rate. More importantly, between the 2D FPT which preserves four properties of the distribution and the 2D FVS schemes by Saha et al. [35] which are relatively easier to implement but preserve only at most two properties of the distribution, it remains to be seen how their differences in formulation affect their performance as far as solving multi-dimensional PBEs is concerned.

In this work, the performances of two state-of-the-art techniques, that is, the FPT [44] and FVS [35] are compared and examined with the aim of providing valuable insights into their numerical capabilities and limitations for solving multi-dimensional breakage PBEs. The two numerical techniques are simultaneously assessed across various performance indicators, namely, time-specific grid-averaged relative number density error, time-averaged relative moments error, and computation time, and are benchmarked against analytical solutions for moments [34,35,47] and, where available, number density [47,48]. In addition, the average size of particles, which is a crucial parameter in processes such as crystallization [23,49,50], is also validated against the analytical solution. Particularly, the 2D breakage scenarios that are evaluated here involve conservation of the first-cross moment or hypervolume (overall size of the particle) and conservation of the first-order moments. For instance, the breakage of high aspect ratio crystals requires careful tracking of the overall size, while conservation of the total mass of fragments during comminution is important. We further assess the capabilities of the techniques in handling both size-independent and size-dependent rate kernels. Our findings reveal that while both FPT and FVS exhibit relatively comparable performances, the ultimate choice of numerical technique is contingent upon the properties that are critical to the breakage process which should be accurately predicted. Insights from this study are pivotal in determining the suitable technique for a reliable multi-dimensional modeling to address the needs of specific breakage problems.

The organization of this paper is as follows: In Section 2, we present the theoretical framework of the FPT and FVS for solving 2D breakage PBEs. Subsequently, in Section 3, we assess the performance of the FPT and FVS for various cases. Conclusions of this study are presented in the last section.

2. Theoretical framework

2.1. Conceptual description of 2D breakage

For a spatially homogeneous system, the continuous 2D pure breakage PBE is given by the following equation [14]:

$$\frac{\partial n(v,w,t)}{\partial t} = \underbrace{\int_w^\infty \int_v^\infty \beta(v,w,v',w')\,\Gamma(v',w')\,n(v',w',t)\,dv'\,dw'}_{\text{Birth of } (v,w) \text{ due to breakage of } (v',w')} - \underbrace{\Gamma(v,w)\,n(v,w,t)}_{\substack{\text{Death of } (v,w) \\ \text{due to breakage} \\ \text{of } (v,w)}} \tag{1}$$

where $n(v,w,t)$ is the number density of particles with internal coordinates (v,w) at time t. For simplicity, the internal coordinates (v,w), which in general can be any two chosen properties that characterize the particles, will be loosely referred to as sizes v and w, each representing a size dimension of the particle. In this context, $\Gamma(v,w)$ is the breakage rate kernel for a particle characterized by size dimensions (v,w), $\beta(v,w,v',w')$ is the stoichiometric kernel which represents the average number of particles formed in the size ranges of v to $v+dv$ and w to $w+dw$ due to the breakage of a parent particle of size dimensions (v',w'), where $v' \geqslant v$ and $w' \geqslant w$.

A conceptual description of 2D breakage is illustrated in Fig. 1. As alluded to earlier, two distinct breakage scenarios will be explored in this work (due to the availability of analytical solutions), i.e., that which conserve the hypervolume and that which conserve the first-order moments. Here, we employ 2D breakage models that involve random quaternary breakage, i.e., $\beta(v,w,v',w') = 4/(v'w')$, for hypervolume conservation and random binary breakage, i.e., $\beta(v,w,v',w') = 2/(v'w')$, for first-order moments conservation. It is worth noting that the properties to be conserved depend on the stoichiometric kernel, $\beta(v,w,v',w')$, which satisfies the constraints shown in Fig. 1. For instance, the conservation of hypervolume requires $\int_0^{w'}\int_0^{v'} v\,w\,\beta(v,w,v',w')\,dv\,dw = v'\,w'$ to hold true. Further, $\int_0^{w'}\int_0^{v'} \beta(v,w,v',w')\,dv\,dw$ is the number of daughter particles produced per breakage event, which would amount to four for quaternary breakage and two for binary breakage.

As an example, if the two internal coordinates of the system represent the length and width of rectangular particles, breakage into four fragments conserves the total area (hypervolume), but not the total length and width (Fig. 1a). Conversely, if particles characterized by two internal properties (e.g., mass and energy, or compositions of two components) undergo binary breakage, the total content of the properties will be conserved (Fig. 1b), which are represented by the first-order moments. Theoretically, the FPT should accurately estimate the conserved properties in both breakage scenarios (Fig. 1a and Fig. 1b) given the formulation encompasses the preservation of four properties in 2D. In contrast, the FVS [35], preserving at most two properties, would require distinct schemes tailored to the two breakage scenarios in Fig. 1.

2.2. General form of discretized 2D pure breakage PBEs

Here we derive the general discretized 2D breakage PBE to accommodate the subsequent discussion on the FPT and FVS. Consider a rectangular 2D mesh in the internal coordinate space (v,w) with a finite domain enclosed by $[v_{\min}, v_{\max}] \times [w_{\min}, w_{\max}]$, as shown in Fig. 2. The 2D domain consists of contiguous rectangular cells denoted by C_{ij}, enclosed by the domain $[v_i, v_{i+1}] \times [w_j, w_{j+1}]$ with $1 \leqslant i \leqslant M_x$, $1 \leqslant j \leqslant M_y$. The 'representative size' within each cell is given by (x_i, y_j), where $v_i < x_i < v_{i+1}$ and $w_j < y_j < w_{j+1}$. It is worth noting that the type of grid used can be flexible and may include uniform or geometric grids. The total number of particles N_{ij} in cell C_{ij}, can thus be obtained by integrating the number density function over the cell limits:

$$N_{ij}(t) = \int_{w_j}^{w_{j+1}} \int_{v_i}^{v_{i+1}} n(v,w,t)\,dv\,dw \tag{2}$$

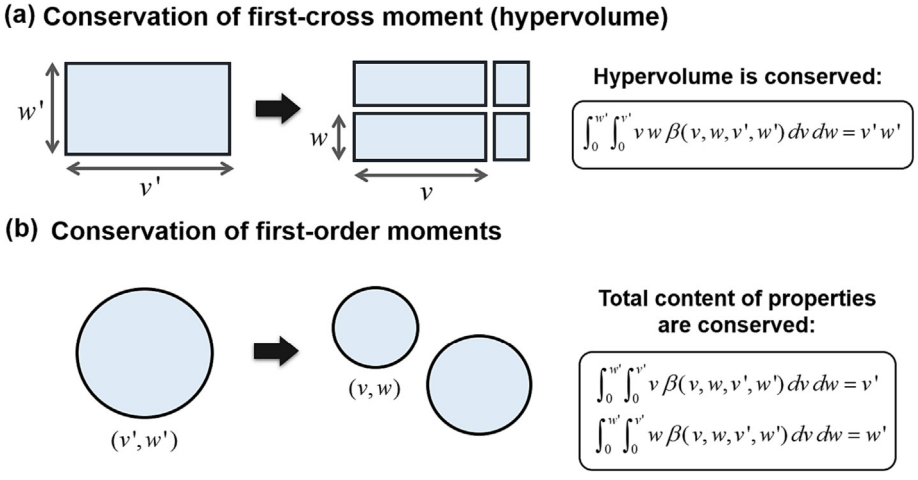

Fig. 1. Example illustrations of 2D breakage for: (a) conservation of hypervolume and (b) conservation of first-order moments, depicting a random quaternary breakage and a random binary breakage, respectively. Here, v and w are the internal coordinates of the system, $\beta(v,w,v',w')$ is the stoichiometric kernel for the breakage of particle of size (v',w'), where $v' \geqslant v$ and $w' \geqslant w$. Note that the chosen internal coordinates need not be size related, as in (b), where they can represent other properties of the particle such as mass and energy content. These entities are expected to be conserved upon binary breakage, as described by the conservation of first-order moments.

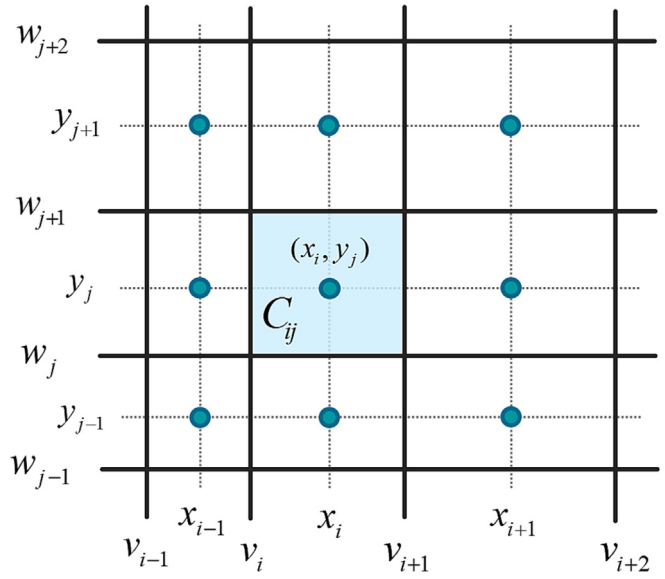

Fig. 2. A rectangular mesh is employed in this work. The solid lines represent the cell limits, and the dots are the pivots. The computational domain is segregated into contiguous rectangular cells C_{ij}, enclosed within $[v_i, v_{i+1}] \times [w_j, w_{j+1}]$, where v and w are the continuous particle sizes, with $1 \leqslant i \leqslant M_x$, $1 \leqslant j \leqslant M_y$. Here M_x and M_y denote the number of cells along horizontal and vertical axes. The 'representative size' in each cell C_{ij} is given by the point (x_i, y_j). Here, $v_i = (x_{i-1} + x_i)/2$ and $w_j = (y_{j-1} + y_j)/2$.

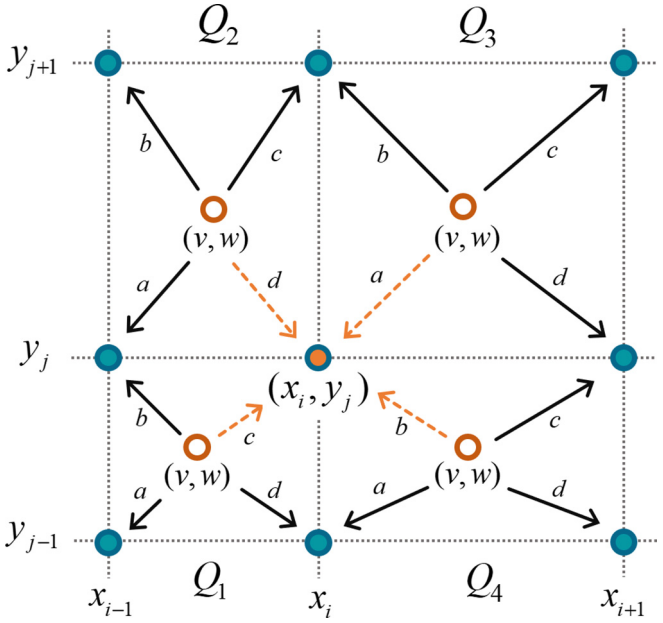

Fig. 3. Fractional assignments a, b, c, and d of the properties associated with non-pivot particle (v, w) to its four neighboring pivots (x, y) on an arbitrary non-uniform grid. Pivot (x_i, y_j) receives an assigning fraction from non-pivot particles (v, w) at each surrounding quadrant, Q_m, where m = 1, 2, 3, 4, as indicated by the dashed arrows.

To discretize $n(v, w, t)$, the particle population in each cell is presumed to be concentrated at the grid point (x_i, y_j), such that the continuous number density function $n(v, w, t)$ can be expressed as follows:

$$n(v, w, t) = \sum_{j=1}^{M_y} \sum_{i=1}^{M_x} N_{ij}(t)\, \delta(v - x_i,\, w - y_j) \tag{3}$$

Integrating both the Left Hand Side (LHS) and Right Hand Side (RHS) of Eq. (1) over the discretized domains from $[v_i, v_{i+1}]$ and $[w_j, w_{j+1}]$, as well as using Eq. (3) will result in the following general discretized PBE for both FPT and FVS:

$$\begin{aligned} \frac{dN_{ij}(t)}{dt} = & \sum_{q=j}^{M_y} \sum_{p=i}^{M_x} \eta_{ijpq}^{num}\, \Gamma_{pq}\, N_{pq}(t) \\ & - \varphi_{ij}^{num}\, \Gamma_{ij}\, N_{ij}(t), \qquad \begin{matrix} i = 1, 2, 3, \ldots, M_x \\ j = 1, 2, 3, \ldots, M_y \end{matrix} \end{aligned} \tag{4}$$

where η_{ijpq}^{num} is the allocation function for particles entering cell C_{ij} due to the breakage of particles characterized by (x_p, y_q) $(p \geqslant i,\ q \geqslant j)$, φ_{ij}^{num} is the allocation function for particles leaving cell C_{ij} due to the breakage of particles characterized by (x_i, y_j), and Γ_{ij} is the breakage rate kernel of particles in cell C_{ij}. The superscript '*num*' denotes the numerical techniques (FPT and FVS). The allocation function η_{ijpq}^{num} and φ_{ij}^{num} will be outlined for the FPT and FVS in the subsequent sections.

2.2.1. Fixed pivot technique (FPT)

The FPT ensures internal consistency within the system with regards to the properties (or moments) of distribution. This is achieved by assigning particles in cell C_{ij} to the neighboring grid points (also called pivots) in such a way that it preserves the moments of interest. Extension of a 1D FPT [44] to 2D FPT using rectangular grids requires the preservation of four properties as particles born within a particular cell are assigned to the four neighboring pivots, as illustrated in Fig. 3.

From Fig. 3, the pivot (x_i, y_j) receives the assigning fractions a, b, c, and d from particles born in the four surrounding quadrants. The assigning fractions can be determined by preserving four chosen properties. Taking a cue from Vale and McKenna [34], the most straightforward selection of properties is the zeroth moment, first-order moments, and the first cross moment. The allocation function is thus:

$$\begin{aligned} \eta_{ijpq}^{FPT} = & \int_{y_{j-1}}^{y_j} \int_{x_{i-1}}^{x_i} \left[\frac{(v - x_{i-1})(w - y_{j-1})}{(x_i - x_{i-1})(y_j - y_{j-1})} \right] \beta(v, w, x_p, y_q)\, dv\, dw \\ & + \int_{y_{j-1}}^{y_j} \int_{x_i}^{x_{i+1}} \left[\frac{(x_{i+1} - v)(w - y_{j-1})}{(x_{i+1} - x_i)(y_j - y_{j-1})} \right] \beta(v, w, x_p, y_q)\, dv\, dw \\ & + \int_{y_j}^{y_{j+1}} \int_{x_{i-1}}^{x_i} \left[\frac{(v - x_{i-1})(y_{j+1} - w)}{(x_i - x_{i-1})(y_{j+1} - y_j)} \right] \beta(v, w, x_p, y_q)\, dv\, dw \\ & + \int_{y_j}^{y_{j+1}} \int_{x_i}^{x_{i+1}} \left[\frac{(x_{i+1} - v)(y_{j+1} - w)}{(x_{i+1} - x_i)(y_{j+1} - y_j)} \right] \beta(v, w, x_p, y_q)\, dv\, dw \end{aligned} \tag{5}$$

For the FPT, $\varphi_{ij}^{FPT} = 1$. Here, $\beta(v, w, x_p, y_q)$ is the stoichiometric kernel for the formation of daughter particles with size (v, w) due to the breakage of parent particles with size (x_p, y_q). Due to the integration range of η_{ijpq}^{FPT} in Eq. (5), FPT implementation requires the first and last pivots in both coordinates of the FPT to be positioned at the minimum and maximum values of the domain, respectively.

2.2.2. Finite volume schemes (FVS)

In this study, the FVS, namely, Scheme 2a and Scheme 2b of Saha et al. [35] are used. The former is devised for breakage that conserves the hypervolume, while the latter is developed for breakage that conserves the first-order moments. In the FVS, weight allocations are implemented in such a way as to preserve the moments of interest during the breakage phenomenon. The allocation functions are given as:

$$\eta_{ijpq}^{FVS} = \Psi_{pq}^{b}\, \mathrm{B}_{ijpq}\, \frac{V_{pq}}{V_{ij}} \tag{6}$$

$$\varphi_{ij}^{FVS} = \frac{\Psi_{ij}^{b}}{\Phi_{ij}} \sum_{n=1}^{M_y} \sum_{m=1}^{M_x} \Phi_{mn} \mathrm{B}_{mnij} \tag{7}$$

where the weight allocation for preserving the properties of interest is defined as:

$$\Psi_{pq}^{b} = \frac{\Phi_{pq}\left[\upsilon_{pq} - 1\right]}{\sum_{n=1}^{q}\sum_{m=1}^{p}\left[\Phi_{pq} - \Phi_{mn}\right]\mathrm{B}_{mnpq}} \tag{8}$$

where $\upsilon_{pq} = \int_0^{y_q} \int_0^{x_p} \beta(v, w, x_p, y_q)\, dv\, dw$ denotes the number of particles produced per breakage event, V_{ij} is the volume of cell C_{ij}, and $\mathrm{B}_{ijpq} = \int_{w_j}^{P_j^q} \int_{v_i}^{P_i^p} \beta(v, w, x_p, y_q)\, dv\, dw$, with $P_i^p = x_i$ and $P_j^q = y_j$ when $p = i$ and $q = j$, otherwise, $P_i^p = v_{i+1}$ and $P_j^q = w_{j+1}$. Here, for the conservation of hypervolume (Scheme 2a), $\Phi_{ij} = x_i y_j$, whereas for the conservation of first-order moments (Scheme 2b), $\Phi_{ij} = x_i + y_j$. Due to the integration range of B_{ijpq}, FVS implementation requires the first grid point in both coordinates to be located within the first cell (not at the minimum value of the domain), while the last grid point of FVS in both coordinates is positioned at the maximum value of the domain.

3. Case study

3.1. Preamble

3.1.1. Model configurations

In this work, we employ a finite domain of internal coordinates v and w of the size range $[v_{\min}, v_{\max}] \times [w_{\min}, w_{\max}] = \left[10^{-9}, 2\right] \times \left[10^{-9}, 2\right]$. In order to account for the steep rise in smaller-sized particles with time, geometric meshing (finer mesh in small-size regions and coarser mesh at large-size regions) is an appropriate choice. For all case studies, unless stated otherwise, by default we employ a geometric mesh with 25×25 grid points (geometric ratio ≈ 3) across the computational domain, and a monodisperse initial distribution, $n(v, w, 0) = \delta(v - v_{\max})\, \delta(w - w_{\max})$, following the general practice in recent numerical studies in the 2D-PBE literature [34,35,38].

It is worth noting that in selecting a finite domain, a finite domain error (FDE) exists, as also raised by Attarakih et al. [51] and Gelbard et al. [52], where particles outside of the domain are not accounted for. Our choice of a monodisperse initial distribution ensures that all particles are initially contained within the finite domain. As a finite domain is inevitable for numerical solutions, the FDE will increase over time as more particles break out of the minimum threshold sizes. In such a situation, the numerical moments will not be able to account for the particles which fall outside the domain and are expected to deviate from the exact moments, which are analytically derived by considering a minimum size threshold of zero, shown below:

$$M_{\lambda\mu}(t) = \int_0^{\infty} \int_0^{\infty} v^{\lambda} w^{\mu} n(v, w, t)\, dv\, dw = \sum_{j=1}^{M_y} \sum_{i=1}^{M_x} x_i^{\lambda} y_j^{\mu} N_{ij}(t) \tag{9}$$

where λ and μ are the orders with respect to v and w.

In Eq. (9), equality only holds when x_1 and y_1 are the non-zero representative sizes for a cell in which the lower cell limits begin with zero. For a finite domain, clearly, x_1 and y_1 are the representative sizes for a cell with non-zero lower limits. In this case, the discretized moments may approximate the theoretical moments only if the minimum size threshold is close to zero or the extent of the production of particles smaller than the minimum size threshold is negligible. Therefore, we adjust the integral limits of the analytical moments to the finite domain used in this study to facilitate an effective comparison with the numerical moments. In this study, all numerical and analytical moments are normalized against the initial analytical moments of identical order.

As the numerical techniques solve directly for N_{ij}, taking a cue from Vale and McKenna [34], we compare the number densities between numerical and analytical solutions in the form of cell average number density. The numerical cell average number density is computed as follows:

$$\bar{n}_{ij}^{num}(t) = \frac{N_{ij}(t)}{\Delta v_i \Delta w_j} \tag{10}$$

where $\Delta v_i = v_{i+1} - v_i$ and $\Delta w_j = w_{j+1} - w_j$. On the other hand, the analytical cell average number density is obtained by integrating the analytical solution over the cell limits and dividing by the grid sizes:

$$\bar{n}_{ij}^{ana}(t) = \frac{1}{\Delta v_i \Delta w_j} \int_{w_j}^{w_{j+1}} \int_{v_i}^{v_{i+1}} n^{ana}(v, w, t)\, dv\, dw \tag{11}$$

where the superscript '*ana*' denotes analytical. Due to the multi-dimensional nature of the problem, visual comparisons of the cell average number densities between numerical and analytical solutions via surface plots are not practical. Therefore, we plot the cell average number densities following the flat representation devised by Chakraborty and Kumar [26], where the quality of solutions can be easily compared in a one-dimensional plot. This is done by first sorting the analytical cell average number density in descending order and assigning a new index (k) to the sorted pivots. The cell average number densities obtained numerically and analytically are then plotted against k and defined as $\bar{n}_k$.

3.1.2. Case studies and performance assessment indicators

We evaluate the performance of the FPT and FVS by testing them against known solutions. As alluded to earlier, two types of breakage phenomena are studied: i) conservation of hypervolume and ii) conservation of first-order moments. Table 1 tabulates the cases along with the exact solutions for moments given by [34,35,38], where the particle count at $t = 0$ is unity with size $(v_{\max}, w_{\max})$.

To quantify the discrepancy between the numerical and analytical cell average number density (applicable to Case 1 only) at a specific time point, t, the following time-specific grid-averaged relative number density error, is used:

$$\varepsilon(t) = \frac{1}{K} \sum_{k=1}^{K} \left| \frac{\bar{n}_k^{ana}(t) - \bar{n}_k^{num}(t)}{\bar{n}_k^{ana}(t)} \right| \tag{12}$$

where K is the total number of pivots/grid points and k is the index of the sorted pivots in descending order of the analytical number density for flat representation. For cases without analytical number density (i.e., Cases 2–4), we are only able to evaluate the performance of the numerical techniques against the analytical moments (Table 1), following the general practice in the 2D-PBM literature [34,35,38]. Correspondingly, the time-averaged relative moments error used for quantifying the discrepancies between the numerical and analytical moments throughout the simulation time duration is given as:

$$\sigma_{\lambda\mu} = \frac{1}{J} \sum_{j=1}^{J} \left| \frac{M_{\lambda\mu}^{ana}(t_j) - M_{\lambda\mu}^{num}(t_j)}{M_{\lambda\mu}^{ana}(t_j)} \right| \tag{13}$$

where J is the total number of time points. In addition to moments, we compute the average size of particles as follows:

$$\bar{v} = \frac{M_{10}}{M_{00}}, \quad \bar{w} = \frac{M_{01}}{M_{00}} \tag{14}$$

Table 1
Cases employed for evaluating the performance of the numerical techniques. $\beta(v,w,v',w')$ is the stoichiometric kernel for particle of size (v,w) due to the breakage of parent particle of size (v',w'), $\Gamma(v,w)$ is the breakage rate kernel for particle of size (v,w), $n^{ana}(v,w,t)$ is the analytical number density of particles of size (v,w) at time t, $M^{ana}_{\lambda\mu}(t)$ is the analytical moments of order λ and μ with respect to v and w, respectively, and v_{max} and w_{max} are the maximum sizes in the computational domain.

Case	$\beta\ (v,\ w,\ v',\ w')$	$\Gamma(v,w)$	Analytical Number Density	Analytical Moments
Conservation of Hypervolume				
1	$\frac{4}{v'w'}$	1	$n^{ana}(v,w,t) = e^{-t}n(v,w,0) + 4te^{-t}\int_w^\infty\int_v^\infty \frac{n(v,w,0)}{v'w'} \sum_{r=0}^\infty \frac{(4t)^r}{(r+1)!(r!)^2}\left[\ln\left(\frac{v'}{v}\right)\ln\left(\frac{w'}{w}\right)\right]^r dv'dw'$	$M^{ana}_{\lambda\mu}(t) = \int_{w_{min}}^{w_{max}}\int_{v_{min}}^{v_{max}} v^\lambda w^\mu n^{ana}(v,w,t)\,dv\,dw$
2	$\frac{4}{v'w'}$	vw	N/A	$M^{ana}_{00}(t) = 1 + 3\,v_{max}w_{max}\,t$ $M^{ana}_{11}(t) = v_{max}w_{max}$
Conservation of First-Order Moments				
3	$\frac{2}{v'w'}$	1	N/A	$M^{ana}_{\lambda\mu}(t) = v^\lambda_{max}w^\mu_{max}\exp\left[\left(\frac{2}{(\lambda+1)(\mu+1)}-1\right)t\right]$
4	$\frac{2}{v'w'}$	$v+w$	N/A	$M^{ana}_{00}(t) = 1 + (v_{max}+w_{max})\,t$ $M^{ana}_{10}(t) = v_{max}$, $M^{ana}_{01}(t) = w_{max}$

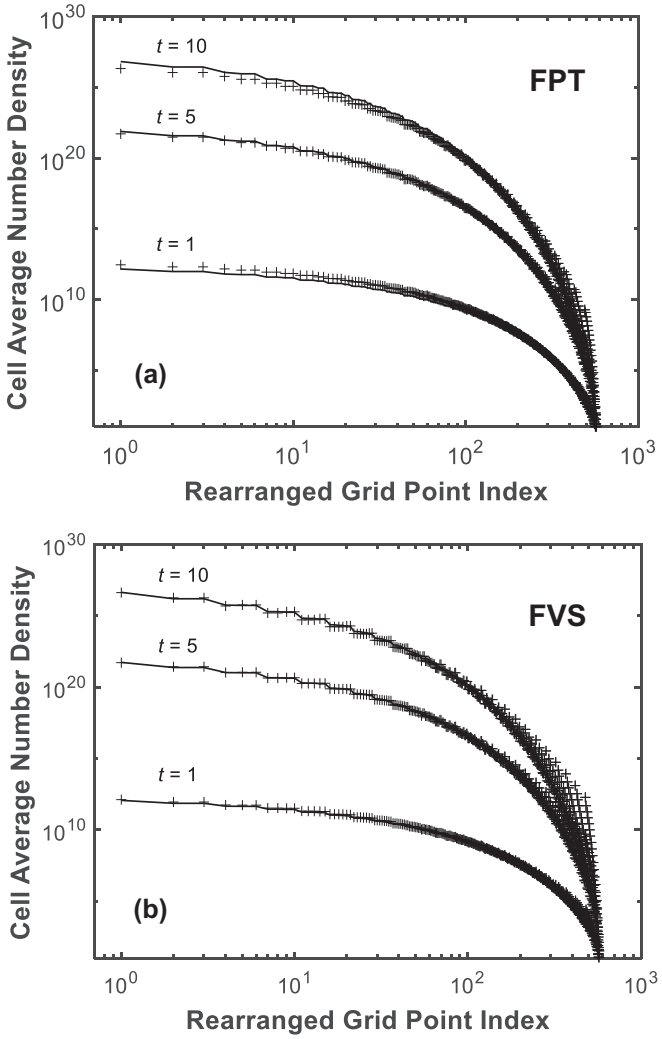

Fig. 4. Case 1 ($\beta(v,w,v',w') = 4/(v'w')$, $\Gamma(v,w) = 1$): A comparison of the cell average number density (Eq. (10)-(11)) predicted by the (a) FPT and (b) FVS (Scheme 2a [35]) against analytical solution using the flat representation [24] on log–log plots. Markers represent the numerical solution and solid lines the analytical solution. The rearranged grid point index is the index of grid points sorted in descending order with respect to the analytical solution. Here, $t = 1$, $t = 5$, and $t = 10$, corresponds to an increase in number of particles by a factor of 2.35e+1, 7.20e+6, and 1.07e+13 relative to the initial condition, respectively. A rectangular grid with 25 geometrically spaced grid points on both internal coordinates (geometric ratio ≈ 3) is used.

Table 2
Time-specific grid-averaged relative errors in the cell average number density, $\varepsilon(t)$ (Eq. (12)), for Case 1 predicted by the FPT and FVS (Scheme 2a [35]) at $t = 1$, $t = 5$, and $t = 10$, corresponding to an increase in number of particles by a factor of 2.35e+1, 7.20e+6, and 1.07e+13 relative to the initial condition, respectively. A rectangular grid with 25 geometrically spaced grid points on both internal coordinates (geometric ratio ≈ 3) is used.

Time, t	$\varepsilon(t)$	
	FPT	FVS
1	0.41	0.50
5	2.69	1.96e+1
10	4.37e+1	6.20e+2

Lastly, we also report the computation time taken in seconds for both numerical techniques to obtain the solution. All computations in this work were carried out using MATLAB® 2022b and the system of ordinary differential equations were integrated using the 'ode15s' sub-routine with a relative tolerance and absolute tolerance of 10^{-6} and 10^{-7}, respectively. The solutions were computed on a workstation equipped with an Intel® Core™ i5-1135G7 CPU with a clock speed of 2.40 GHz and 16 GB of installed memory (RAM).

3.2. 2D pure breakage with hypervolume conservation

3.2.1. Case 1: Size-Independent breakage

In Case 1, a breakage scenario which conserves the hypervolume, M_{11}, is considered. Here, the stoichiometric kernel, i.e., $\beta(v,w,v',w') = 4/(v'w')$, admits a breakage phenomenon in which a particle undergoes random breakage into four fragments. When the breakage rate is size-independent, i.e., $\Gamma(v,w) = 1$, all particles break at an equal rate, which results in a significant number of particles falling out of the minimum size threshold. As such, the FDE would increase rapidly over time due to failure to account for particles outside of the finite domain.

The numerical cell average number densities obtained by both the FPT and FVS (Scheme 2a [35]) are shown in Fig. 4 for three different times: $t = 1$, $t = 5$, and $t = 10$, corresponding to an increase in number of particles by a factor of 2.35e+1, 7.20e+6, and 1.07e +13 relative to the initial condition, respectively. Although both techniques show good predictions, a noticeable overprediction is present at smaller populations at the right most side of the plot, which tends to intensify with the extent of breakage. Interestingly, the overprediction appears to be more significant in the FVS as compared to the FPT. This is also quantitatively reflected in Table 2, where the time-specific grid-averaged relative number density error of the FVS grows rapidly in comparison to those of the FPT. The overprediction can likely be attributed to the use of rectangular grids. In the case of FPT, the preservation of four properties in

Table 3
Time-specific grid-averaged relative errors in the cell average number density, $\varepsilon(t)$ (Eq. (12)), for Case 1 predicted by the FPT and FVS (Scheme 2a [35]) at $t = 10$ with different number of geometrically spaced grid points.

Grids	$\varepsilon(t)$	
	FPT	FVS
25×25	4.37e+1	6.20e+2
30×30	2.71e+1	5.42e+2
35×35	1.70e+1	4.05e+2

2D causes non-pivot particles to deviate from the expected size, as highlighted by Chakraborty and Kumar [26] and Nandanwar and Kumar [27]. Similar implications may be said about the FVS in terms of the utilization of weight allocations within a rectangular space. Refining the mesh is one way to improve the prediction, which evidently entails higher computational expense as seen in Table 3. Other strategies include employing triangular grids [26] or radial grids [27], where they have been proven to enhance the numerical solution substantially.

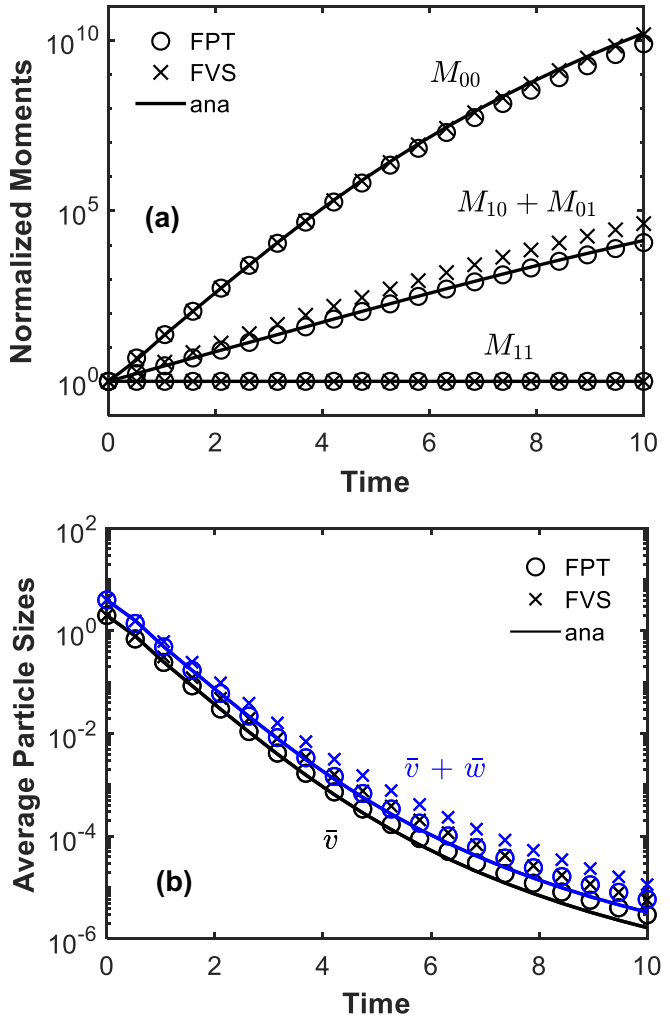

Fig. 5. Case 1 ($\beta(v,w,v',w') = 4/(v'w')$, $\Gamma(v,w) = 1$): A comparison between the FPT and FVS (Scheme 2a [35]) against the analytical solution (within the finite domain) in predicting the (a) moments of distribution $M_{\lambda\mu}$ of order λ and μ with respect to v and w, respectively, and (b) average particle sizes on semi-log plots. In (b), different colors are used to distinguish the average particle size, $\bar{v}$ (which is also equivalent to $\bar{w}$ for this case), and the total average particle size, $\bar{v}+\bar{w}$. The moments are normalized against the initial analytical moments of identical order. Here, $t = 10$ corresponds to an increase in number of particles by a factor of 1.07e+13. A rectangular grid with 25 geometrically spaced grid points on both internal coordinates (geometric ratio ≈ 3) is used.

Notably, we also observe that the FVS predicts the number density more accurately than the FPT in regions with larger number densities, as observed at the left most region of the plot (Fig. 4). From Fig. 4a, at $t = 1$, a slight overprediction is seen in the number density computed by the FPT, where most particles are still concentrated at the larger size regions. As breakage proceeds ($t = 5$), the FPT solution at larger number densities improves, but subsequently underpredicts at $t = 10$. This suggest that FVS would be a more appropriate choice if number density at higher populations (which is typically the smaller size particles in breakage processes) is a highly critical parameter, whereas FPT would be suitable if accurate prediction of number densities for the overall populations is required. In many applications involving fine particle production via grinding, such as the food packaging industry, the number densities of fine polymer particles are highly essential to the application [53].

Next, we assess the performance of the numerical techniques in computing the moments of distribution. As alluded to previously, the numerical moments for this case will be benchmarked against the analytical moments computed within the finite domain of the grid used in this study (Table 1) for an objective comparison to eliminate the impact of FDE. As observed in Fig. 5a, the FVS predicts the zeroth moment excellently, while the FPT pales in comparison. Due to the extensive breakage in this case, the number density is highly steep at the small size regions during extended times. Consequently, the FPT would require more pivots to capture the total number of particles, whereas the FVS performs well even with a coarse mesh, as seen in Table 4. Both numerical techniques conserve the hypervolume M_{11}, with the FPT attaining a lower error $\sim O(10^{-5})$ as compared to FVS with $\sim O(10^{-1})$ (Table 4). When it comes to estimating the first-order moments (M_{10} and M_{01}), the FPT demonstrates exceptional performance (Fig. 5a), but the FVS tends to overpredict these quantities over time. This is expected given that the FVS (Scheme 2a of Saha et al. [35]) was designed to only preserve the hypervolume and the zeroth moment. Not surprisingly, the situation improves with mesh refinement, as shown in Table 4. In summary, the FVS outperforms in estimating the zero moment, the FPT excels in predicting the first-order moments, and both techniques are comparable and excellent in capturing the hypervolume.

The accuracy of the moments significantly influences the average size of particles estimated by the techniques. Fig. 5b highlights the superior performance of the FPT in predicting both the average particle size, $\bar{v}$ (which is also equivalent to $\bar{w}$ for this case), and total average particle size, $\bar{v}+\bar{w}$, compared to the FVS. This is not surprising, as the high error margins in the first-order moments by the FVS result in poor estimation of the average size of particles, despite its excellent prediction in the zeroth moment. Therefore, the FPT is the obvious choice for accurate modeling when more than two moments should be accurately estimated, such as in crystallization of high aspect-ratio crystals where the mean crystal sizes, e.g., mean length and mean width, are critical properties of the system. Notably, the formulation of FPT has the flexibility in preserving higher-order moments, such as the volume of crystals, e.g., M_{12} [23,49], while the FVS requires extensive redesign. Conversely, the FVS is the more economical choice for simple applications requiring only accurate prediction of zero moments and hypervolume.

3.2.2. Case 2: Size-dependent breakage

Here, we further assess the performance of the numerical techniques in tackling size-dependent breakage, $\Gamma(v,w) = vw$, for the same stoichiometric kernel as Case 1, i.e., $\beta(v,w,v',w') = 4/(v'w')$.

Table 4
Time-averaged relative errors in the moments of order λ and μ with respect to v and w, respectively, $\sigma_{\lambda\mu}$ (Eq. (13)), for Case 1 predicted by the FPT and FVS (Scheme 2a [35]) up to $t = 10$ using different number of geometrically spaced grid points.

Grids	FPT			FVS		
	σ_{00}	$\sigma_{10}+\sigma_{01}$	σ_{11}	σ_{00}	$\sigma_{10}+\sigma_{01}$	σ_{11}
15×15	4.34e−1	9.46e−2	4.24e−5	1.59e−1	2.61e+1	1.88e−1
20×20	3.06e−1	5.13e−2	4.24e−5	9.16e−2	1.39e+1	1.88e−1
25×25	2.20e−1	3.20e−2	4.24e−5	5.61e−2	8.58	1.88e−1
30×30	1.64e−1	2.18e−2	4.24e−5	3.66e−2	6.30	1.88e−1
35×35	1.27e−1	1.58e−2	4.24e−5	2.49e−2	5.18	1.88e−1

Due to the absence of an analytical solution for number density, we benchmark the numerical moments against their analytical solutions in Table 1. In this breakage scenario, larger particles break at more rapid rates than smaller ones resulting in negligible FDE compared to Case 1, thus enabling the comparative assessment of the moments. The solution is evaluated up until $t = 10$, corresponding to an increase in number of particles by a factor of 1.21e+2.

Fig. 6 shows that the FPT and FVS (Scheme 2a [35]) exhibit excellent agreement with analytical moments, indicating their remarkable accuracy in predicting the moments. Considering the less extensive breakage for this case, the grid employed is sufficient for FPT to capture the zeroth moment accurately, as opposed to that in Case 1. We further test the numerical computations using different meshes and both the FPT and FVS demonstrate comparable accuracies for this case. The time-averaged relative errors for the zeroth moment, σ_{00}, using the FPT and FVS are $\sim$O(10^{-8}) and $\sim$O(10^{-9}), respectively, while the errors for the first-order moments, σ_{10}+σ_{01}, are $\sim$O(10^{-15}) and $\sim$O(10^{-16}), respectively. These findings indicate that both methods are suitable for accurately modeling such breakage processes.

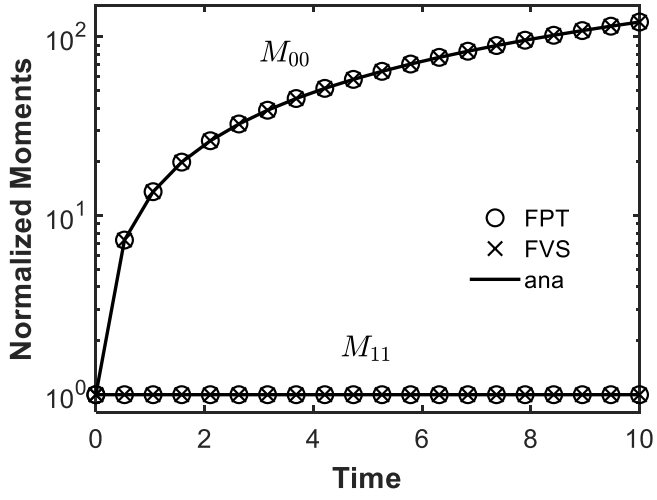

Fig. 6. Case 2 ($\beta(v,w,v',w') = 4/(v'w')$, $\Gamma(v,w) = vw$): A comparison between the FPT and FVS (Scheme 2a [35]) against the analytical solution in predicting the moments of distribution $M_{\lambda\mu}$ of order λ and μ with respect to v and w, respectively, on a semi-log plot. The moments are normalized against the initial analytical moments of identical order. Note that the analytical solution for first-order moments is not available, hence not shown in plot. Here, $t = 10$ corresponds to an increase in number of particles by a factor of 1.21e+2. A rectangular grid with 25 geometrically spaced grid points on both internal coordinates (geometric ratio $\approx$ 3) is used.

3.3. 2D pure breakage with first-order moments conservation

3.3.1. Case 3: Size-independent breakage

Breakage with conservation of first-order moments, M_{10} and M_{01}, involves a stoichiometric kernel of $\beta(v,w,v',w') = 2/(v'w')$, where a particle undergoes random breakage into two fragments. The extent of breakage is less extensive as compared to Case 1.

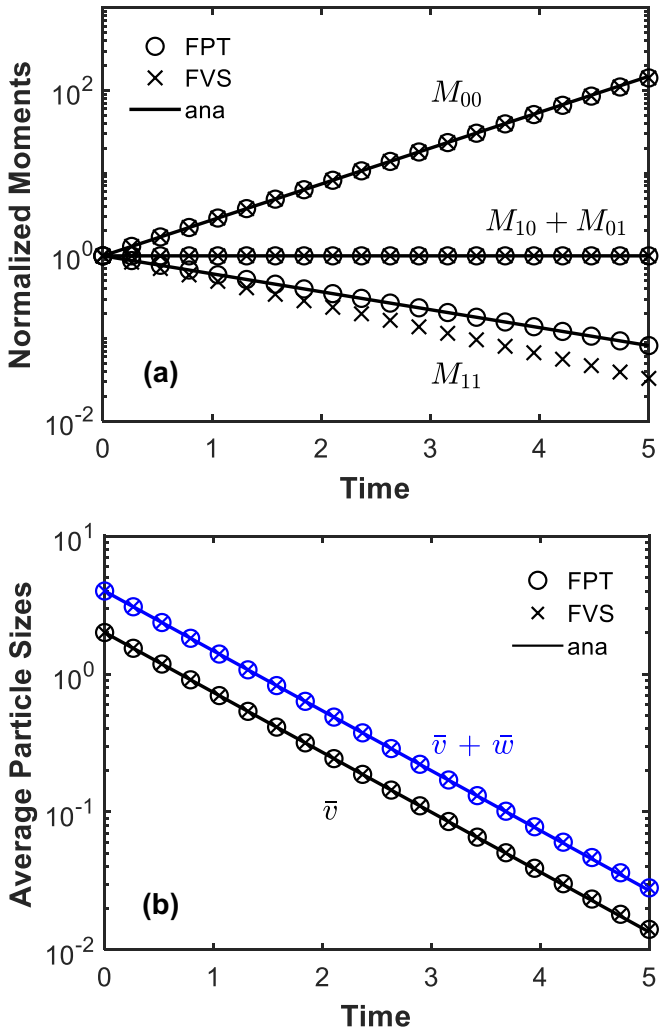

Fig. 7. Case 3 ($\beta(v,w,v',w') = 2/(v'w')$, $\Gamma(v,w) = 1$): A comparison between the FPT and FVS (Scheme 2b [35]) against the analytical solution in predicting the (a) moments of distribution $M_{\lambda\mu}$ of order λ and μ with respect to v and w, respectively, and (b) average particle sizes on semi-log plots. In (b), different colors are used to distinguish the average particle size, $\bar{v}$ (which is also equivalent to $\bar{w}$ for this case), and the total average particle size, $\bar{v}+\bar{w}$. The moments are normalized against the initial analytical moments of identical order. Here, $t = 5$ corresponds to an increase in number of particles by a factor of 1.48e+2. A rectangular grid with 25 geometrically spaced grid points on both internal coordinates (geometric ratio $\approx$ 3) is used.

For a size-independent breakage, particles are expected to fall out of the minimum size threshold at extended times. In the absence of analytical number density, we compare the numerical moments with the exact moments tabulated in Table 1 but plotted the results up until $t = 5$ (increase in number of particles by a factor of 1.48e+2) to minimize the impact of FDE on the comparative assessment.

Fig. 7a shows that both the FPT and FVS (Scheme 2b [35]) predict the zeroth moment satisfactorily, demonstrating similar performance with σ_{00} ~O(10^{-3}) across different meshes. Notably, the FVS outperforms the FPT in predicting the first-order moments, with σ_{10}+σ_{01} ~O(10^{-13}) compared to the FPT, with σ_{10}+σ_{01} ~O(10^{-5}). This can be attributed to the intrinsic characteristic of the FVS (Scheme 2b of Saha et al. [35]), as it was designed to preserve the first-order moments. Consequently, the average size and total average size of particles are well predicted by both techniques, as seen in Fig. 7b. However, the FVS shows poor accuracy in predicting the hypervolume M_{11}, with σ_{11} ~O(10^{-1}), as also reported in [35], whereas the FPT achieves an error of σ_{11} ~O(10^{-8}), indicating better performance. This is expected as the FVS Scheme 2b [35] was designed to preserve only the first-order and zeroth moments, thus compensating for the accuracy of other moments. Therefore, while the FVS schemes are simple to implement with reasonable accuracy, distinct schemes (Scheme 2a for Cases 1–2 and Scheme 2b for Cases 3–4) are necessary for different conservation requirements. Moreover, as alluded to earlier, the FVS is limited to preserving only two properties of choice and compromises the accuracy of other moments. In this regard, the FPT, despite its slightly added complexity, can be tailored to suit different conservation scenarios, making it well-suited for general usage. In contrast, where only the first-order moments and average particle sizes are important, the FVS is adequate for such applications.

3.3.2. Case 4: Size-dependent breakage

Finally, we evaluate the performance of the FPT and FVS (Scheme 2b [35]) in handling size-dependent breakage for the same breakage phenomenon as Case 3. The solution is computed up until time $t = 10$, which corresponds to an increase in number of particles by a factor of 4.10e+1. The moments of distribution are depicted in Fig. 8. While the FPT shows good agreement with the analytical zeroth moment with σ_{00} ~O(10^{-4}), the FVS, interestingly, exhibits a slight underprediction with σ_{00} ~O(10^{-2}) at extended times. Further, quantitative results indicate that the FVS outperforms the FPT in predicting the hypervolume moments with σ_{10}+σ_{01} ~O(10^{-15}), compared to that of FPT at σ_{10}+σ_{01} ~O(10^{-4}). Nevertheless, both techniques show promising competencies and would be adequate to model breakage processes of this type.

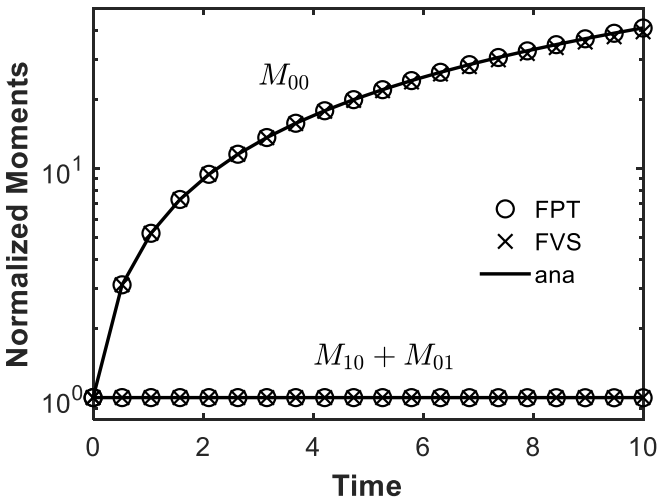

Fig. 8. Case 4 ($\beta(v, w, v', w') = 2/(v'w')$, $\Gamma(v, w) = v + w$): A comparison between the FPT and FVS (Scheme 2b [35]) against the analytical solution in predicting the moments of distribution $M_{i,\mu}$ of order λ and μ with respect to v and w, respectively, on a semi-log plot. The moments are normalized against the initial analytical moments of identical order. Note that the analytical solution for hypervolume is not available, hence not shown in plot. Here, $t = 10$ corresponds to an increase in number of particles by a factor of 4.10e+1. A rectangular grid with 25 geometrically spaced grid points on both internal coordinates (geometric ratio ≈ 3) is used.

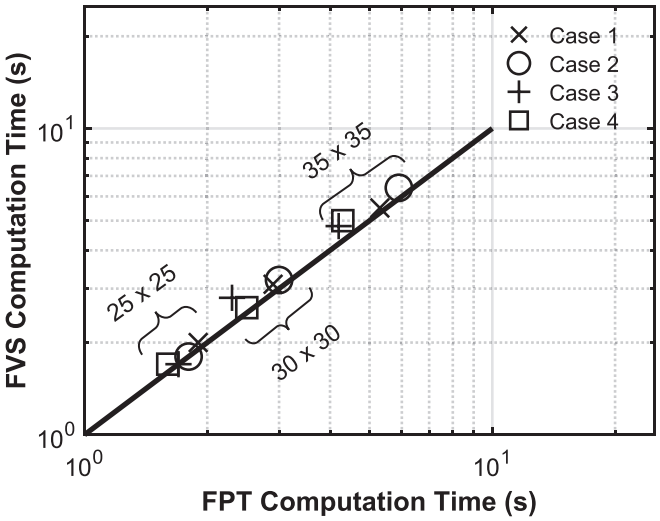

Fig. 9. A comparison of the computation times in seconds of the FPT and FVS with increasing number of grid points, i.e., 25 × 25, 30 × 30, and 35 × 35, for the four cases on a log–log plot. The solutions were computed using MATLAB® 2022b on a workstation equipped with Intel® Core™ i5-1135G7 CPU with a clock speed of 2.40 GHz and 16 GB of installed memory (RAM),

3.4. Computation time

To observe the computation times between the FPT and FVS, we plot the computation times for all four cases with increasing number of grid points, i.e., 25 × 25, 30 × 30, 35 × 35, as shown in Fig. 9. It is evident that the computation times associated with both techniques are comparable, with the ratio between their respective times approaching unity. Although the FVS is relatively simpler to implement compared to the FPT, both techniques show similar computational efficiency. With more refined mesh, e.g., 100 × 100, both techniques took on average of ~ 55 mins to compute the solutions up to t = 10 for all test cases. Therefore, being able to resolve the equations accurately and swiftly (within seconds) using a coarser mesh such as that shown in our case studies will benefit situations which require the multi-dimensional PBEs to be resolved repeatedly, e.g., during parameter estimation with a genetic algorithm, or deployment in model predictive control.

4. Conclusions

Two state-of-the-art numerical techniques, i.e., the FPT and FVS, have established a reputation as promising strategies for tackling higher-order PBEs. In this work, we evaluate the performance of the FPT and FVS in solving pure breakage 2D-PBEs and validate the results against analytical solutions. We considered two types of 2D breakage scenarios: (i) breakage with conservation of the first-cross moment (hypervolume) and (ii) breakage with conservation of the first-order moments, both with size-independent

and size-dependent rate kernels. Our results reveal that, while both the FPT and FVS exhibit relatively comparable accuracy in predicting the number densities and in their computation times, the selection of numerical technique hinges on the properties/moments that necessitate precise estimation. When up to two important moments are critical for observation, the FVS is the preferred option attributing to its simpler formulation, although necessitating distinct schemes for conserving different properties (e.g., Scheme 2a for hypervolume conservation and Scheme 2b for first-order moments conservation). Moreover, the selection of moment conservation in the FVS is also contingent upon the specific breakage function/mechanism. In contrast, the slightly more complex FPT offers versatility by effectively balancing accuracy and the ability to preserve up to four properties in the internal 2D space, rendering it adequate for general usage. Further, for the conservation of other properties, the FPT formulation is flexible in adapting to the properties of choice, whereas the FVS requires redesign. Equipped with an understanding of the capabilities of numerical techniques in solving multi-dimensional breakage PBM, we can anticipate an increased utilization of the population balance model for precise control over the dynamics of multi-dimensional particles across a diverse range of applications.

Declaration of Competing Interest

The authors declare that they have no known competing financial interests or personal relationships that could have appeared to influence the work reported in this paper.

Data Availability

MATLAB codes to produce the results in this study are available on request from the authors.

Acknowledgements

We would like to acknowledge the financial support in the form of Fundamental Research Grant Scheme (FRGS/1/2020/TK0/MUSM/03/1) from the Ministry of Higher Education Malaysia (MOHE), of which Yong Kuen Ho is the principal investigator. We also thank Monash University Malaysia for the financial support to Suet Lin Leong.

References

[1] F. Ahamed, M. Singh, H.-S. Song, P. Doshi, C.W. Ooi, Y.K. Ho, On the use of sectional techniques for the solution of depolymerization population balances: results on a discrete-continuous mesh, Adv. Powder Technol. 31 (2020) 2669–2679.
[2] S.I.X. Tiong, F. Ahamed, H. Sitaraman, S.L. Leong, Y.K. Ho, Modeling simultaneous particle shrinkage, dissolution and breakage using the modified moving grid technique, Powder Technol. 421 (2023) 118439.
[3] Y.K. Ho, P. Doshi, H.K. Yeoh, Modelling simultaneous chain-end and random scissions using the fixed pivot technique, Can. J. Chem. Eng. 96 (2018) 800–814.
[4] Y.K. Ho, P. Doshi, H.K. Yeoh, G.C. Ngoh, Modeling chain-end scission using the Fixed Pivot technique, Chem. Eng. Sci. 116 (2014) 601–610.
[5] D. Barrasso, A. El Hagrasy, J.D. Litster, R. Ramachandran, Multi-dimensional population balance model development and validation for a twin screw granulation process, Powder Technol. 270 (2015) 612–621.
[6] A. Dan, H. Vaswani, A. Šimonová, R. Ramachandran, Multi-dimensional population balance model development using a breakage mode probability kernel for prediction of multiple granule attributes, Pharm. Dev. Technol. 28 (2023) 638–649.
[7] C. Frances, A. Liné, Comminution process modeling based on the monovariate and bivariate direct quadrature method of moments, AIChE J. 60 (2014) 1621–1631.
[8] A. Das, S. Bhoi, D. Sarkar, J. Kumar, Sonofragmentation of rectangular plate-like crystals: bivariate population balance modeling and experimental validation, Cryst. Growth Des. 20 (2020) 5424–5434.
[9] J. Shojaeiarani, D. Bajwa, G. Holt, Sonication amplitude and processing time influence the cellulose nanocrystals morphology and dispersion, Nanocomposites 6 (2020) 41–46.
[10] A. Schaum, P. Jerono, P. Feketa, Robust impulsive observer design for infinite-dimensional cell population balance models, Int. J. Robust Nonlinear Control 32 (2022) 774–791.
[11] Y. Qi, A.U. Mohammad Masuk, R. Ni, Towards a model of bubble breakup in turbulence through experimental constraints, Int. J. Multiph. Flow 132 (2020) 103397.
[12] Á. Borsos, B.G. Lakatos, Influence of breakage on crystal size distribution in a continuous cooling crystallizer, Period. Polytech., Chem. Eng. 56 (2012) 65.
[13] C.Y. Ma, K.J. Roberts, Morphological population balance modelling of the effect of crystallisation environment on the evolution of crystal size and shape of para-aminobenzoic acid, Comput. Chem. Eng. 126 (2019) 356–370.
[14] D. Ramkrishna, Population Balances: Theory and Applications to Particulate Systems in Engineering, Elsevier Science & Technology, San Diego, San Diego, 2000.
[15] D. Ramkrishna, A.W. Mahoney, Population balance modelling. Promise for the future, Chem. Eng. Sci. 57 (2002) 595–606.
[16] D. Ramkrishna, M.R. Singh, Population balance modeling: current status and future prospects, Ann. Rev. Chem. Biomol. Eng. 5 (2014) 123–146.
[17] Á. Borsos, B. Lakatos, Investigation and simulation of crystallization of high aspect ratio crystals with fragmentation, Chem. Eng. Res. Des. 92 (2014) 1133–1141.
[18] H. Briesen, Simulation of crystal size and shape by means of a reduced two-dimensional population balance model, Chem. Eng. Sci. 61 (2006) 104–112.
[19] F. Puel, G. Févotte, J.P. Klein, Simulation and analysis of industrial crystallization processes through multidimensional population balance equations. Part 2: a study of semi-batch crystallization, Chem. Eng. Sci. 58 (2003) 3729–3740.
[20] T. Rosenbaum, V. Mbachu, N.A. Mitchell, J.F. Gamble, P. Cho, J.D. Engstrom, Comparison of one-dimensional and two-dimensional population balance models for optimization of a crystallization process for a needle-shaped active pharmaceutical ingredient, Org. Process Res. Dev. 26 (2022) 1094–1105.
[21] K. Sato, H. Nagai, K. Hasegawa, K. Tomori, H.J.M. Kramer, P.J. Jansens, Two-dimensional population balance model with breakage of high aspect ratio crystals for batch crystallization, Chem. Eng. Sci. 63 (2008) 3271–3278.
[22] M. Shoji, H. Takiyama, The application of two-dimensional population balance model to study the effect of temperature profile on the crystal size distribution and aspect ratio, Cryst. Growth Des. 12 (2012) 5241–5246.
[23] B. Szilágyi, A. Eren, J.L. Quon, C.D. Papageorgiou, Z.K. Nagy, Monitoring and digital design of the cooling crystallization of a high-aspect ratio anticancer drug using a two-dimensional population balance model, Chem. Eng. Sci. 257 (2022) 117700.
[24] S.L. Leong, S.I.X. Tiong, S.P. Siva, F. Ahamed, C.-H. Chan, C.L. Lee, I.M.L. Chew, Y. K. Ho, Morphological control of cellulose nanocrystals via sulfuric acid hydrolysis based on sustainability considerations: an overview of the governing factors and potential challenges, J. Environ. Chem. Eng. 10 (2022) 108145.
[25] A.H. Alexopoulos, C. Kiparissides, Solution of the bivariate dynamic population balance equation in batch particulate systems: combined aggregation and breakage, Chem. Eng. Sci. 62 (2007) 5048–5053.
[26] J. Chakraborty, S. Kumar, A new framework for solution of multidimensional population balance equations, Chem. Eng. Sci. 62 (2007) 4112–4125.
[27] M.N. Nandanwar, S. Kumar, A new discretization of space for the solution of multi-dimensional population balance equations: simultaneous breakup and aggregation of particles, Chem. Eng. Sci. 63 (2008) 3988–3997.
[28] M.N. Nandanwar, S. Kumar, A new discretization of space for the solution of multi-dimensional population balance equations, Chem. Eng. Sci. 63 (2008) 2198–2210.
[29] H.M. Vale, T.F. McKenna, Solution of the population balance equation for two-component aggregation by an extended fixed pivot technique, Ind. Eng. Chem. Res. 44 (2005) 7885–7891.
[30] J. Kumar, M. Peglow, G. Warnecke, S. Heinrich, The cell average technique for solving multi-dimensional aggregation population balance equations, Comput. Chem. Eng. 32 (2008) 1810–1830.
[31] R. Kumar, J. Kumar, G. Warnecke, Numerical methods for solving two-dimensional aggregation population balance equations, Comput. Chem. Eng. 35 (2011) 999–1009.
[32] S. Bhoi, D. Sarkar, Hybrid finite volume and Monte Carlo method for solving multi-dimensional population balance equations in crystallization processes, Chem. Eng. Sci. 217 (2020).
[33] G. Kaur, J. Kumar, S. Heinrich, A weighted finite volume scheme for multivariate aggregation population balance equation, Comput. Chem. Eng. 101 (2017) 1–10.
[34] J. Saha, A. Bück, Conservative finite volume schemes for multidimensional fragmentation problems, Mathematics 9 (2021).
[35] J. Saha, N. Das, J. Kumar, A. Bück, Numerical solutions for multidimensional fragmentation problems using finite volume methods, Kinetic Relat. Models 12 (2019) 79–103.
[36] M. Singh, H.Y. Ismail, R. Singh, A.B. Albadarin, G. Walker, Finite volume approximation of nonlinear agglomeration population balance equation on triangular grid, J. Aerosol Sci. 137 (2019).
[37] M. Singh, R. Singh, S. Singh, G. Singh, G. Walker, Finite volume approximation of multidimensional aggregation population balance equation on triangular grid, Math. Comput. Simul. 172 (2020) 191–212.

[38] M. Singh, T. Matsoukas, V. Ranade, G. Walker, Discrete finite volume formulation for multidimensional fragmentation equation and its convergence analysis, J. Comput. Phys. 464 (2022) 111368.
[39] R. Dürr, A. Bück, Approximate moment methods for population balance equations in particulate and bioengineering processes, Processes 8 (2020) 414.
[40] D.E. Rosner, R. McGraw, P. Tandon, Multivariate population balances via moment and monte carlo simulation methods: an important sol reaction engineering bivariate example and "Mixed" moments for the estimation of deposition, scavenging, and optical properties for populations of nonspherical suspended particles, Ind. Eng. Chem. Res. 42 (2003) 2699–2711.
[41] D.E. Rosner, S. Yu, MC simulation of aerosol aggregation and simultaneous spheroidization, AIChE J. 47 (2001) 545–561.
[42] M. Singh, V. Ranade, O. Shardt, T. Matsoukas, Challenges and opportunities concerning numerical solutions for population balances: a critical review, J. Phys. A: Math. Theor. 55 (2022) 383002.
[43] S. Kumar, D. Ramkrishna, On the solution of population balance equations by discretization—II. A moving pivot technique, Chem. Eng. Sci. 51 (1996) 1333–1342.
[44] S. Kumar, D. Ramkrishna, On the solution of population balance equations by discretization—I. A fixed pivot technique, Chem. Eng. Sci. 51 (1996) 1311–1332.
[45] M. Singh, G. Walker, Finite volume approach for fragmentation equation and its mathematical analysis, Numer. Algorithms 89 (2022) 465–486.
[46] S. Kumar, D. Ramkrishna, A general discretization technique for solving population balance equations involving bivariate distributions, in: AIChE Annual Meeting, Miami Beach, FL, USA, 1995, pp. 17.
[47] G.J. Rodgers, M.K. Hassan, Fragmentation of particles with more than one degree of freedom, Phys. Rev. E 50 (1994) 3458–3463.
[48] P. Singh, M.K. Hassan, Kinetics of multidimensional fragmentation, Phys. Rev. E 53 (1996) 3134–3144.
[49] B. Szilágyi, Z.K. Nagy, Aspect ratio distribution and chord length distribution driven modeling of crystallization of two-dimensional crystals for real-time model-based applications, Cryst. Growth Des. 18 (2018) 5311–5321.
[50] M. Singh, S. Shirazian, V. Ranade, G.M. Walker, A. Kumar, Challenges and opportunities in modelling wet granulation in pharmaceutical industry – a critical review, Powder Technol. 403 (2022) 117380.
[51] M.M. Attarakih, H.J. Bart, N.M. Faqir, Optimal moving and fixed grids for the solution of discretized population balances in batch and continuous systems: droplet breakage, Chem. Eng. Sci. 58 (2003) 1251–1269.
[52] F.M. Gelbard, J.H. Seinfeld, Coagulation and growth of a multicomponent aerosol, J. Colloid Interface Sci. 63 (1978) 472–479.
[53] J. Schmidt, M. Plata, S. Tröger, W. Peukert, Production of polymer particles below 5μm by wet grinding, Powder Technol. 228 (2012) 84–90.